THIN FILM TRANSISTORS: ATOMIC LAYER DEPOSITION OF HIGH-K SBOX AT LOW TEMP

Madhujya Gogoi,
Assistant Professor, Department of Physics,
Dhemaji College, Dhemaji, Assam

ABSTRACT
At low temperatures, SbOx thin films are produced using atomic layer deposition (ALD) employing antimony reactants SbCl5 and Sb(NMe2)3 and oxidizers H2O and H2O2. SbCl5 reacts with both oxidizers, but no deposition is seen when Sb(NMe2)3 and H2O are used. For the first time, the reaction process and dielectric characteristics of ALD-SbOx thin films are examined in detail. These films display a strong breakdown field of 4 MV cm1, a high areal capacitance of 150–200 nF cm2, and a dielectric constant of 10–13. The ZnO semiconductor layer is effectively incorporated into a SbOx dielectric layer, resulting in the fabrication of thin film transistors (TFTs). A TFT with a SbOx dielectric layer formed at 200 °C from Sb(NMe2)3 and H2O2 exhibits outstanding performance, including a field effect mobility () of 12.4 cm2 V1 s1, an Ion/Ioff ratio of 4 108, a subthreshold swing of 0.22 V dec1, and a trapping state (Ntrap) of 1.1 1012 eV1 cm2. SbOx's amorphous structure and high areal capacitance enhance the interfaces between the semiconductor and dielectric layer of TFT devices, creating a strong electric field for electrons, hence increasing device mobility.

KEYWORDS: Atomic Layer Deposition, High-*K* Dielectric, Low Temperature, Oxide Semiconductor, ToF-ERDA

1. INTRODUCTION

The number of research focusing on metal oxide thin films has increased significantly in recent years owing to their huge potential for usage as insulators or semiconductors. [1–2] Thin film transistors (TFTs) constructed on oxide thin films have been extensively explored to date due to their superior electrical characteristics, high uniformity, and transparency. [3] As demand for high-performance electronics increases, standard low-k materials such as SiO2 are unable to keep up, resulting in serious device reliability difficulties. [4] According to the generalised capacitance equation, C = 0rS/d, where 0, r, S, and d denote the dielectric constant of free space, the relative dielectric constant, the area, and the depth of the dielectric, respectively, a high-k dielectric substance would be able to supply strong capacitive coupling while also scaling down to device size (below 100 nm). Additionally, the increased capacitance of a high-k dielectric enables enough charge input into the TFT semiconductor layer, enhancing the device's performance. Over the last decade, a variety of dielectrics with high k values (>9), such as zirconium dioxide (ZrO2), aluminium oxide (Al2O3), hafnium oxide (HfO2), neodymium oxide (Nd2O3), and yttrium oxide (Y2O3), have been investigated as potential candidates to replace the conventional SiO2 gate dielectric in TFTs (Figure 1). Al2O3 was one of the earliest materials explored as a possible alternative to SiO2 as a gate dielectric. Al2O3 is completely suitable with the analogous metal–oxide–semiconductor structure because to its higher bandgap. [6] Additionally, Hf-based dielectrics have been presented as potentially useful materials for large-scale integration. Intel declared in 2007 that Hf-based high-k materials will be utilised in 45 nm manufacturing, the world's first commercial manufacture of high-k materials. [7] Additionally, Zeumault and Subramanian demonstrated that by employing ZrO2 as a booster gate dielectric through a thermally induced emissive method, the mobility of ZnO TFTs may be significantly increased. [8] However, the number of high-k dielectrics available today is still restricted, and new high-k materials candidates must be researched further. Antimony oxide was recently described as a novel dielectric material owing to its excellent dielectric properties. [9] For a dielectric layer thickness of 100 nm, the breakdown field may approach 2.5 MV cm1. [10] Liu et al. demonstrated that "monolayer molybdenum disulfide field-effect transistors" supported on a Sb2O3 dielectric substrate display much less transfer-curve hysteresis than those supported on a SiO2 dielectric substrate. [11] However, it should be noted that at high concentrations, Sb2O3 is recognised as a carcinogen.
Details are included in the caption that follows the picture.

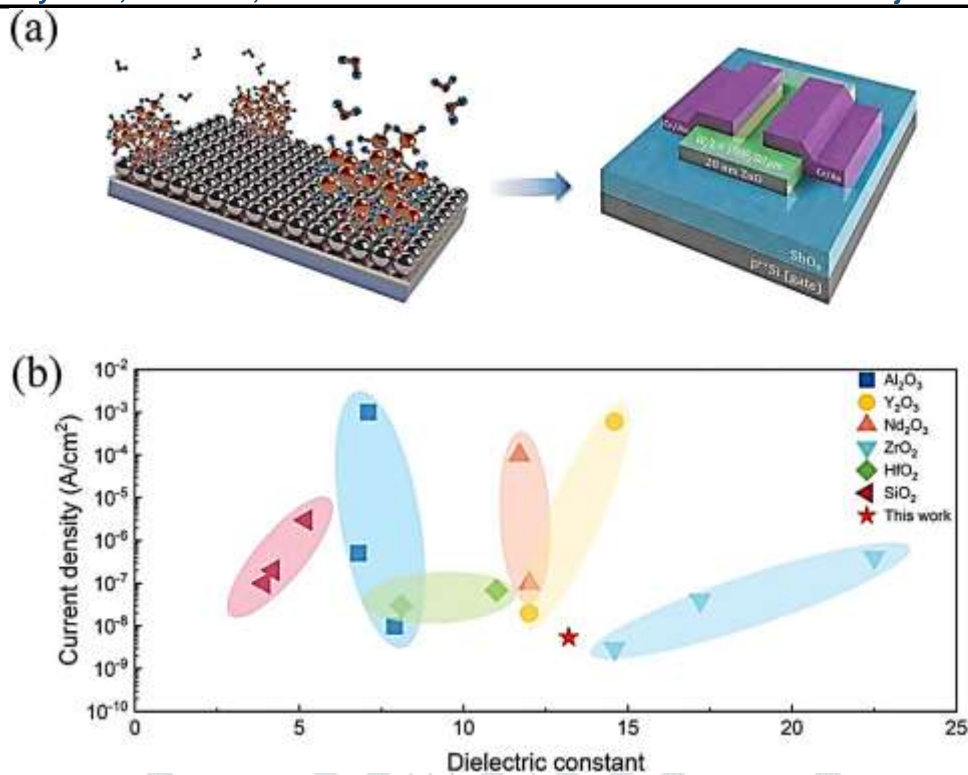

Fig 1: a) Process flow diagram from thin film to device. b) A summary of the dielectric characteristics of materials with a high dielectric constant. [20, 19].

Apart from the constitution of metal oxides, the process of thin film production is critical for developing high-performance devices. Surface scattering and degradation of device stability may occur when thin films are produced using magnetron sputtering and pulsed laser deposition processes. Furthermore, solution-deposited thin films (such as sol–gel and inkjet printing) need very high post annealing temperatures to generate a high-density metal–oxygen–metal (MOM) structure. Additionally, repeatability is not always achieved sufficiently in these films. [13] The electrical characteristics of TFT devices are strongly impacted by the flaws at the interface between the channel and the insulator, as well as the layer roughness. [14] It is widely established that an electrical device's optimal operation requires a dielectric substance with a smooth surface. [1] For example, despite their high dielectric constant, conventional high-k thin films such as ZrO2 and HfO2 are prone to producing a rough surface crystal structure. [15] Additionally, the dielectric property of a high-k layer is highly dependent on the preparation procedure, which heavily influences the impurity and residue groups present in the material structure. [16] As a result, it is critical to choose a deposition technology that is highly reproducible, has great thickness controllability, precise chemical composition control, and grows at low temperatures.

Due to sequential and self-limiting surface reactions, the atomic layer deposition (ALD) approach has the greatest conformality of all deposition techniques and atomic layer control across a large deposition temperature range.

[17] ALD is frequently employed in the coating of metal oxide thin films because to its great conformability. To our knowledge, the dielectric characteristics of SbOx produced through ALD have never been investigated. We fabricate SbOx dielectric thin films using thermal ALD at low temperatures (80–200 °C) utilising SbCl5 and Sb (NMe2)3 as antimony reactants and H2O and H2O2 as oxidizers. We explored the electrical and structural characteristics of deposited SbOx sheets in detail. The flat surface of the amorphous structure of SbOx produced in this work results in a high-quality dielectric/semiconductor interface. Additionally, the dielectric constant of SbOx is greater than 13, resulting in a capacitance that is adequate. Additionally, the elemental concentration in the films was determined using time-of-flight elastic recoil detection analysis (ToF-ERDA) to establish a correlation between the impurity level and device performance. Additionally, the ALD ZnO semiconductor material was incorporated into a SbOx dielectric and used to manufacture a TFT device due to its nontoxicity, cheap cost, and high mobility features. The ALD method is shown in this work to provide a good interface state between the channel and insulator, hence improving the performance of TFT devices. As a result, ALD-processed SbOx is an excellent option for future study and development as a novel high-k material.

2. RESULTS AND DISCUSSION

To better understand the development behaviour of SbOx thin films and the influence of various precursors on their quality and performance, H2O and H2O2 oxidants were used to interact with SbCl5 and Sb(NMe2)3. The proposed process is shown in Figure 2. The hydroxyl-soaked surface is exposed to the Sb precursor, which interacts with the hydroxyl group, forming a hydroxyl terminated surface with a Cl (or CH3) termination. The surface of the Cl (or CH3) will be exposed to an oxygen source (H2O2 or H2O) and will react to form one layer of a SbOx thin film. Each half ALD cycle eliminates excess precursors and by-products through the carrier gas.

Details are in the caption following the image

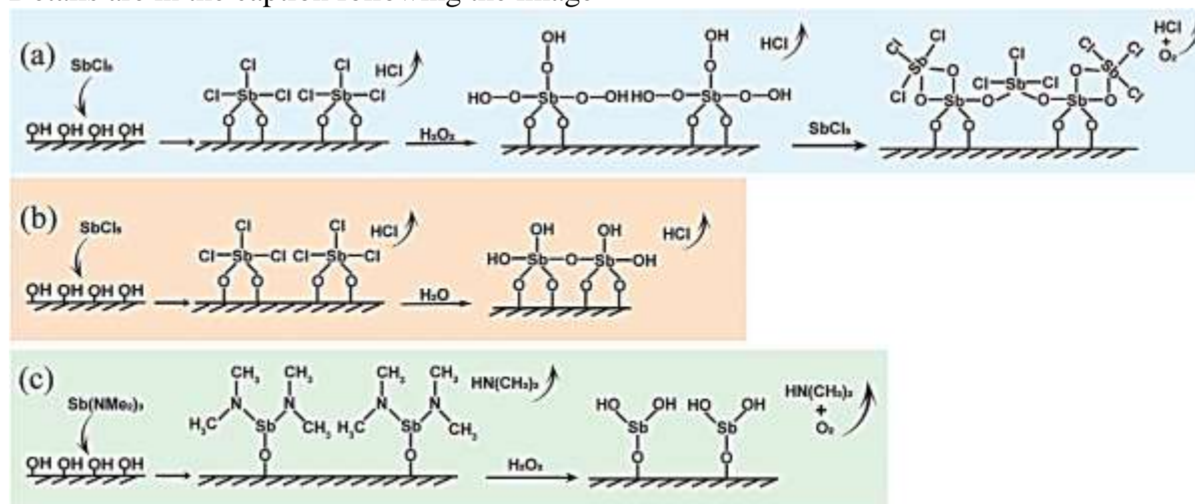

Figure 2: Schematic diagram of the reaction mechanism for ALD SbOx using different precursors: SbCl5 and a) H2O2 or b) H2O, c) Sb(NMe2)3 and H2O2.

The growth parameters of SbOx with regard to various precursors at various compartment temperature are depicted in Figure 3. Figures S1 and S2 (Supporting Information) illustrate the thickness and X-ray reflectivity (XRR) patterns, respectively. The growth per cycle (GPC) of all thin films diminishes as the deposit temperature (TD) rises. This is most likely owing to the desorption of reactive surface sites on the substrate, such as OH, at higher temperatures. [21] When a sufficient number of Sb precursors is pulsed into the chamber and the surface reaction is unrestricted, the amount of OH groups on the surface is critical for controlling the ALD growth rate. Thus, when the TD increases, the density of OH drops, resulting in a decrease in the GPC. [22] It should be noted that SbOx deposited using SbCl5 and various oxygen sources has a very variable growth rate. For instance, the GPC of SbOx (SbCl5 + H2O) is 1.3, but only 0.9 for SbOx generated by the reaction of SbCl5 and H2O2. The quantity of surface hydroxyl groups substantially relies on the vapour pressure of the oxidant precursor, as per the Langmuir adsorption isotherm. [23] At ambient temperature, the vapour pressure of H2O2 is 18.4 Torr, which is less than that of H2O (23.8 Torr). Due to the comparatively low density of OH groups, SbOx with SbCl5 and H2O2 has a lower GPC.

Details are in the caption following the image

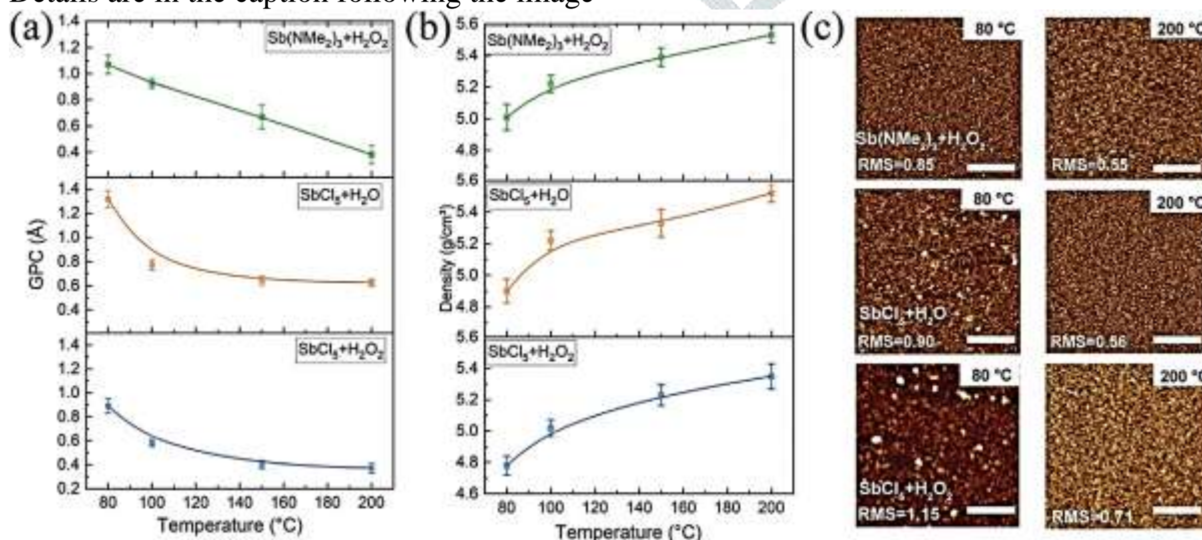

Figure 3: a) The growth rate, b) density, and c) AFM images (scale bar: 1 μm) of the SbOx thin films.

Figure 3b shows the density values for the thin films derived from the estimated fit to the XRR patterns. The density of the SbOx thin films rises with increasing TD, from 4.9 g cm3 at 80 °C to 5.5 g cm3 at 200 °C. In this situation, impurity incorporation caused by a faster growth rate, as well as partial detachment of chemical legends during the purging process owing to a lower deposition temperature, may influence thin film density. As illustrated in Figure 3c and Figure S3, the surface morphologies of SbOx were investigated using atomic force microscopy (AFM) investigations with scanned areas of 5 5 m2 (Supporting Information). The root mean squared value of the surface is somewhat greater for SbOx films produced using SbCl5 than for Sb (NMe2)3. The discrepancies in the obtained surface roughness can be attributed to several factors, including the following: I film grown using metal chloride precursors always require a "incubation" period, imposing a limited number of ALD cycles to achieve uniform protection of a hydrogen-terminated Si surface, which can result in difficulty with initiating cycles and a high degree of surface roughness,[24] and ii) films grown using metal chloride precursors always require a "incubation" period. ii) the creation of HCl as a by-product, which etches the thin layers, resulting in a rough and non-uniform surface. [25]

Figures S4 and S5 illustrate the scanning electron microscopy (SEM) images (Supporting Information). There is a distinct contact between the thin films deposited and the Si substrate. As previously stated, inhomogeneous SbOx deposition occurs when Sb(NMe2)3 and H2O are employed as precursors, most likely due to H2O's low oxidising capacity (Figure S5e, Supporting Information). At a TD of 80 °C, 900 cycles of SbOx deposition using Sb(NMe2)3 and H2O2 resulted in a thickness of 106.2 nm, which decreases to 36.6 nm at 200 °C, which is compatible with the XRR data. The transmission electron microscopy (TEM) analysis (Figure S5c, Supporting Information) and grazing incidence X-ray diffraction patterns (Figure S5d, Supporting Information) patterns confirm the amorphous nature of all SbOx thin films deposited using various precursors at the deposition temperatures investigated.

The bonding energy and molecular states of the components in the SbOx thin films shown in Figure 4a–d and Figure S6 were determined using XPS (Supporting Information). To calibrate the bonding affinity, the C 1s state was employed as a reference. Figure 4b depicts the normalised O 1s area. The thin film formed at 200 °C has a lower O 1s area than other films, which is compatible with the study of Sb's coordination number change. Interestingly, as TD increased, the XPS peaks shifted toward lower binding energies. Two methods may account for this phenomenon: I the gradual oxidation of Sb from SbOCl [or Sb(NMe2)2OH] to SbOx,[26] and ii) the reduction of Sb's coordination number (from Sb2O5 to Sb2O3) might result in a drop in binding energy. [27] Although the O 1s and Sb 3d spectra overlap, some tight constraints allow for the separation of the O 1s and Sb 3d spectra;[28] I 3d3/2 has the same complete width at half maximum as 3d5/2, ii) the centre distance between 3d5/2 and 3d3/2 is 9.34 eV, and iii) 3d5/2 has a potentially 1.5 times greater area than 3d3/2. It is well established that during ALD, a strong MCl (M is the metal atom) link can seldom be replaced by a MO bond. A high TD is required to overcome this large activation energy barrier, as shown by first principle calculations. [29] Additionally, a high TD may significantly limit the amount of Cl contaminants incorporated into the produced film [25] (see Figure S7 in the Supporting Information).

Details are in the caption following the image

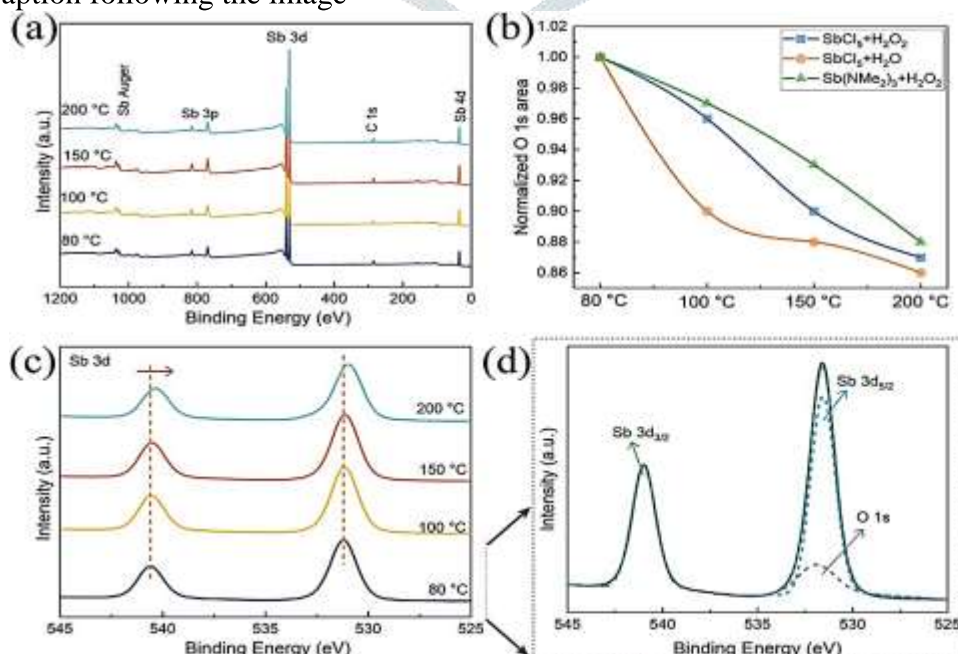

Figure 4 a) XPS survey for Sb 3d for SbOx thin films (Sb(NMe2)3 and H2O2). b) Normalized O 1s area. c) Sb 3d spectra and d) fitting result.

F-ERDA analysis was utilised to identify several elements in the SbOx thin films, including Sb, O, H, C, and Cl, as seen in Figure 5a–d and Table 1. Certain contaminants, like as H, may have a significant effect on the performance of TFT devices. [20] While it is commonly assumed that an excess of hydrogen in the dielectric layer of TFTs degrades performance of the device as a result of the generation of surplus carriers, a governed amount of hydrogen can proficiently passivate the electrode/SbOx interfacial states and form an electric double layer, resulting in a high areal capacitance. [30] As a result, accurate H content monitoring is critical for ALD films generated using hydrogen-containing precursors. ToF-ERDA outperforms X-ray photoelectron spectroscopic analysis in terms of sensitivity and depth resolution, and time-of-flight secondary ion mass spectrometry in form of numerical evaluation capabilities, making it ideal for detecting trace amounts of H, Cl, and C, as well as the Sb:O ratio in the SbOx film. The ERDA measurements indicate that the Sb/O ratio rises as the deposition temperature increases. The similar trend was seen for hydrogen content when deposition temperature was increased, i.e., hydrogen content decreased from 11.2% to 0.6% when the deposition temperature of SbOx using Sb (NMe2)3 and H2O2 was increased from 80 to 200 °C. Additionally, substances deposited at lower temperatures (80 °C) were not stable and were partly damaged by the ion beam during the measurement, resulting in some uncertainty in the ERDA analysis findings for these samples. Table 1 provides a more complete breakdown of the constituent content of all deposited films.

Details are in the caption following the image

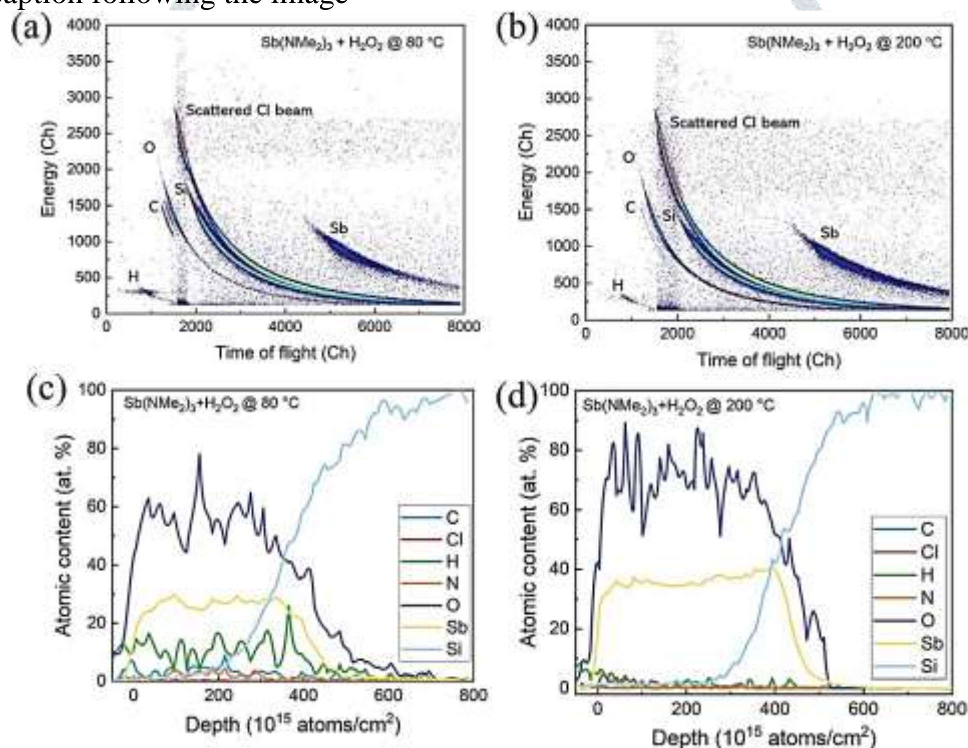

Figure 5: ERDA spectrum of ALD SbOx deposited at a) 80 °C and b) 200 °C using Sb(NMe2)3 and H2O2. At the two-dimensional histogram of raw spectra, light components are more prominent in the bottom left corner of the figure, where energy and time of flight are at their lowest values. Each element's lower energy and longer time-of-flight suggest that the events originate farther from the sample. c,d) ERDA depth profile of SbOx on a Si substrate, derived using the Potku software programme after examining the spectra presented.

Table 1. Elemental compositions of ALD-grown films determined by ToF-ERDA

Sample	T_D [□C]	*H* [at%]	*C* [at%]	Cl [at%]	N [at%]	Sb [at%]	Sb:O
$SbCl_5$ H_2O_2	□80	22 □2	0.3 □0.06	1 □0.3	—	25 □2	0.52
	200	3.2 □1.5	0.3 □0.15	0.8 □0.3	—	34.5 □1.5	0.56
$SbCl_5$ H_2O	□80	19 □2	0.6 □0.2	1.5 □0.5	—	25 □2	0.48
	200	5.5 □1.5	0.1 □0.08	0.9 □0.3	—	31 □3	0.51
$Sb(NMe_2)_3$ □H_2O_2	80	11.2 □2	4.0 □1.0	—	2.4 □0.8	26.5 □1.5	0.47
	200	0.6 □0.3	0.22 □0.07	—	0.13 □0.06	33 □2	0.53

To characterise the optical characteristics of the deposited SbOx films, they were developed on a quartz glass substrate, as seen in Figure 6a and Figure S8 (Supporting Information). The thin films are very transparent in the visible region, at 80%, as shown by the optical picture in the inset figure, which favours their use in transparent electrical devices. The bandgap values found for SbOx deposited using various precursors are variable. It is found that when the TD is raised, the bandgap values rise (Figure S8, Supporting Information). Soon and colleagues used density functional theory to determine the band structure of SbOx. [31] They discovered that when the SbOx phase transitions from Sb2O5 to Sb2O3, the bandgap rises significantly. SbOx is a blend of Sb2O5 (low bandgap) and Sb2O3 in our work (high bandgap). The Sb:O ratio determined by ToF-ERDA (Table 1) and XPS (Figure 4b) indicates that the phase is mostly Sb2O3 with a somewhat larger bandgap. By raising the temperature of deposition and decreasing the coordination number of Sb, we may produce more Sb2O3 and hence a larger bandgap.

Details are in the caption following the image

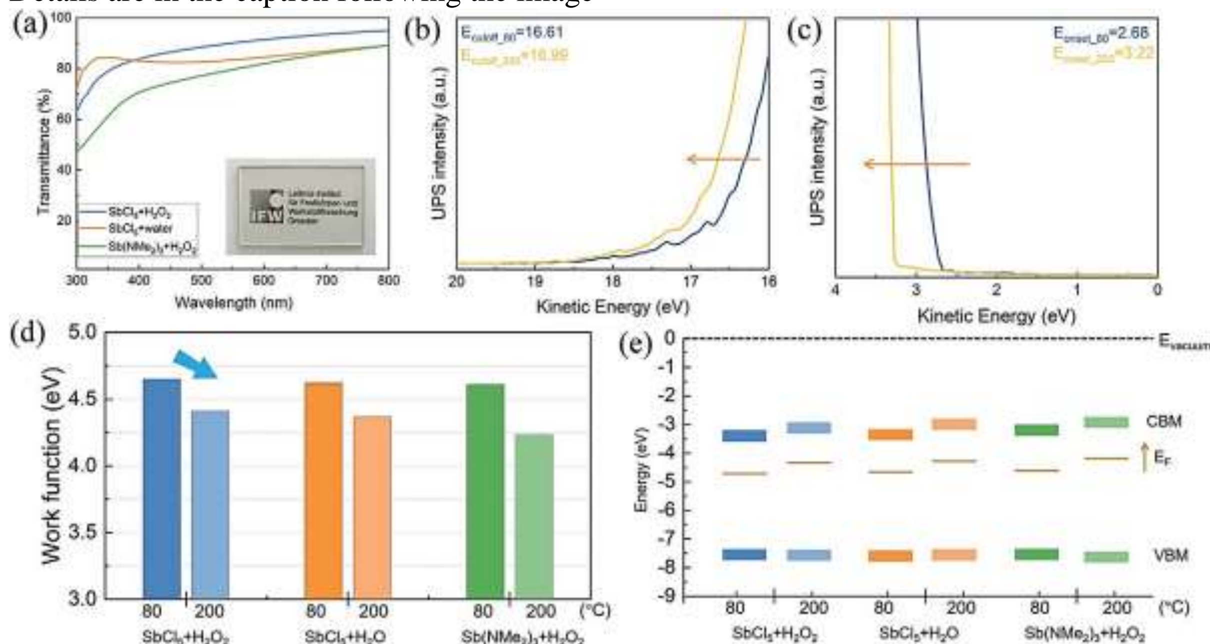

Figure 6: a) Transmittance of SbOx developed at a temperature of 200 °C. UPS spectra of a SbOx thin film produced using Sb(NMe2)3 and H2O2 were obtained for b) the secondary electron onset and c) the valence band edge. d) For all SbOx thin films, the work function and e) the band structure diagram are shown.

UV photoelectron spectroscopy (UPS) in conjunction with XPS offers information on the electrical architecture and energy band locations of diverse materials. UPS spectra were acquired in order to investigate the band structure of SbOx thin films. In all three systems, raising the deposition temperature results in a distinct shift of the secondary electron cutoff (Ecutoff) and valence band edge to higher energies, as seen in Figure 6b,c and Figure S9 (Supporting Information). The work function () was derived by subtracting the secondary cutoff energy from the photon energy (21.2 eV) and is shown in Figure 6d. The findings demonstrate that has decreased as a consequence of increasing deposition temperature and the Fermi level's shift closer the conduction band edge. In their analysis of the Ba0.5Sr0.5TiO3 system, Kumar and colleagues observed the similar phenomena. [32] Due to the produced vacancies, the orbital character is disrupted, resulting in a Fermi level shift toward the conduction band. Another possibility is that amorphous Sb2O3 is more n-type than Sb2O5. [33] As previously stated, when the deposition temperature was increased, the thin films phase transitioned from Sb2O5 to Sb2O3, as shown by ToF-ERDA (Table 1) and XPS (Figure 4b) findings. Thus, the availability of more Sb2O3 phase in the thin film at elevated temperatures may result in a greater proximity of the Fermi level to the conduction band. The appropriate valence band maximum has been determined, and the related energy band diagram is shown in Figure 6e. According to previous findings, an offset for may occur as a consequence of differing process conditions and composition change. [34] We hypothesise that the drop in the coordination number of Sb (from Sb2O5 to Sb2O3) with increasing temperature might result in a decrease in.

The electrical and dielectric characteristics of ALD SbOx thin films produced using various precursors and deposition temperatures were evaluated using metal–insulator–metal structured capacitors. The leakage current behaviour of the SbOx dielectrics is shown in Figure 7a and Figure S10 (Supporting Information). All SbOx thin films formed at 80 °C exhibit a considerable leakage current density (Figure S10, Supporting Information). At

lower deposition temperatures, the thin films have a high concentration of impurities due to partial breakdown of the precursors (see Table 1), which operate as leakage current pathways and contribute to the high current density. At higher deposition temperatures, a decreased leakage current may indicate complete decomposition of precursors and, consequently, fewer impurities in the final deposited film, which is consistent with the density obtained values using XRR analyses and the impurity content determined using the ToF-ERDA method. Additionally, at a deposition temperature of 200 °C, the current density and breakdown field of films developed with Sb(NMe2)3 are lower than those formed with SbCl5 (Figure 7a), indicating a larger density of traps in the metal–oxide framework of films generated from chlorine-based precursors. Kukli et al. found that films formed from chlorine-based precursors had a larger trap density than films generated from other precursors,[35] results in higher current density and a lower breakdown field. The capacitance–frequency characteristics of the SbOx dielectric produced at 200 °C with various predecessors are shown in Figure 7b. The SbOx thin film formed by Sb(NMe2)3 has a dielectric constant of around 13.2. (Figure S10d, Supporting Information).

Details are in the caption following the image

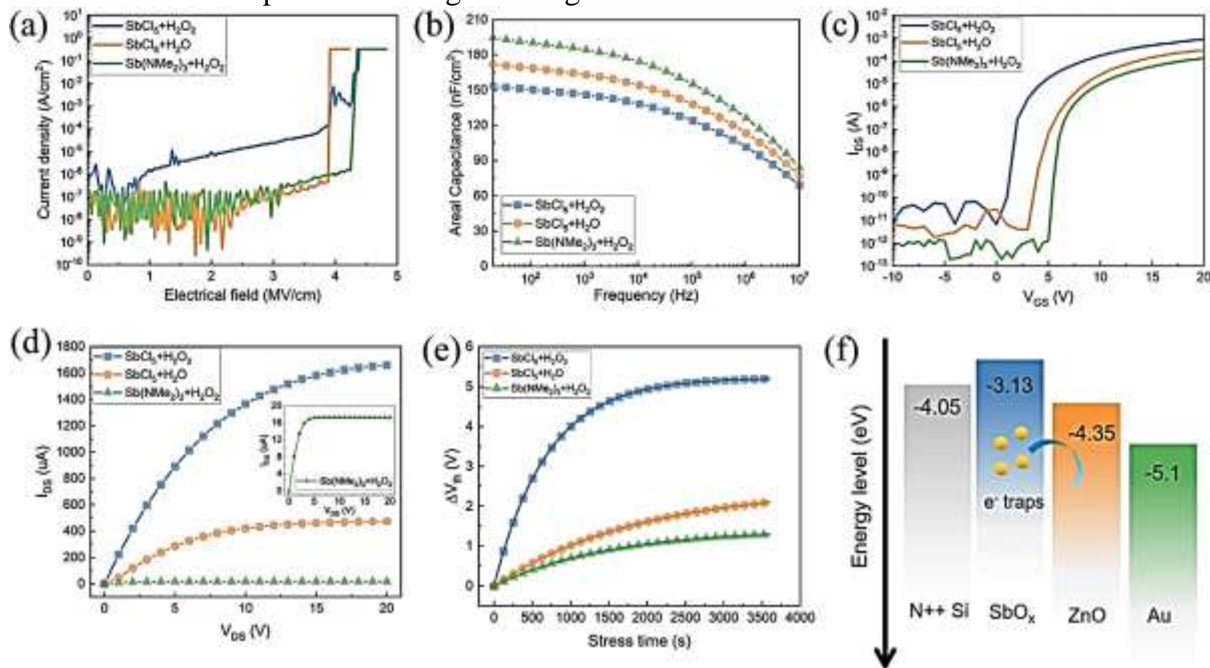

Figure 7: a) Characteristics of the leakage current density and b) capacitance frequencies of SbOx dielectrics deposited at 200 °C c) ZnO/SbOx thin film transistor transfer curves. d) Output curve for a 20 V fixed gate voltage. d) Results of a positive bias stress test. f) Diagram illustrating the metal–insulator–semiconductor electron emission pathway.

To obtain low leakage current TFTs, the minimum offset of the dielectric conduction band compared to the semiconductor material in an n-type transistor should be at least 1 eV. [36] During the device measurement, a band offset greater than 1 eV effectively limits the charges inside the ZnO channel (Figure S11, Supporting Information). To demonstrate the viability of using SbOx thin films as a dielectric layer in TFTs, bottom-gated TFTs were merged with an ALD ZnO channel layer. Figure 7c illustrates typical transfer curves. Table 2 summarises the critical electrical parameters. The slope of TFTs based on the Sb(NMe2)3 precursor was determined using the derivative of the transfer curve. A high field-effect mobility of 12.4 cm2 V1 s1 and a low subthreshold swing (SS) value of 0.22 V dec1 were calculated. However, the TFT based on the SbOx dielectric produced from SbCl5 exhibits suboptimal performance, with a mobility of 6.3 cm2 V1 s1 and an SS value of 0.88 V dec1. Additionally, the max areal density of states (Ntrap) was calculated using the following formula [37] using the SS data.

$SS = kBT\ \ln\ 10q[1 + q2Cox Ntrap]$ (1)

Here, kB denotes Boltzmann's constant, T denotes Kelvin temperature, Cox denotes gate oxide capacitance, and q denotes electron charge. As shown in Table 2, SbOx was produced from Sb (NMe2)3- and H2O2-based TFTs with a low Ntrap value, suggesting a good interface between the channel layer (ZnO) and dielectric layer (SbOx). [20] The output characteristics of TFTs are shown in Figure 7d, clearly exhibiting pinch-off behaviour and drain current saturation at high VDS.

Table 2. Performance characteristics for ZnO/SbOx TFTs using ZnO as the channel and SbOx as the dielectric layer (, Vth, Ion/Ioff, SS, and Ntrap denote the field-effect mobility, threshold voltage, on/off current ratio, subthreshold swing, and trapping state).

Precursors	V_{th} [V]	μ [cm^2 V□1 s□1]	Ion/Ioff	SS [V dec□1]	Ntrap [eV□1 cm□2]
$SbCl_5$ and H_2O_2	2.57	6.3	5 □10^7	0.88	7.5 □10^{12}
$SbCl_5$ and H_2O	4.72	8.7	2 □10^7	0.65	3.7 □10^{12}
$Sb(NMe_2)_3$ and H_2O_2	5.03	12.4	4 □10^8	0.22	1.1 □10^{12}

Electrical stability is also determined under long-term positive bias stress (PBS), which is accomplished by introducing a steady positive bias (+20 V) between the drain and source for 1 hour and then analysing the transfer curve (Figure S12, Supporting Information). When a positive voltage is given to the ZnO semiconductor under ambient circumstances, electrons collect. The electronegativity of the surrounding oxygen molecules allows them to collect electrons from the conduction band, forming O2 species. As a result, the ZnO layer's carriers may be eliminated, resulting in a change in the positive threshold voltage (Vth). [20] Figure 7e and Figure S13 illustrate the energy band diagram for TFTs under PBS circumstances, as well as the fluctuations in the threshold voltage shift (Vth) as a function of stress time (Supporting Information). As can be seen, the TFT based on SbCl5 and H2O2 exhibits a greater voltage shift of 5.1 V, but the TFT based on Sb(NMe2)3 exhibits a voltage shift of just 1.2 V, indicating that there are only a few flaws at the semiconductor-dielectric layer contact.

Different factors may account for the better performance of TFTs depending on the Sb(NMe2)3 precursor. To begin, chlorine is a highly electronegative contaminant that impairs the dielectric performance of SbOx thin films significantly. The SbOx thin film formed from the Sb(NMe2)3 precursor, on the other hand, has a low impurity level, indicating a reduced density of states. Second, the amorphous structure has smoother surfaces than the crystalline structure, which results in a high-quality dielectric/semiconductor contact. Additionally, the smooth contact reduces surface scattering, which improves the efficiency of TFT devices. [38] Thirdly, it is hypothesised that SbOx dielectrics produced at low temperatures form inherent donor-like electron traps. The traps inject electrons into the ZnO semiconductor through thermally induced emission, hence raising the electron concentration in bulk ZnO and resulting in a high field-effect mobility in TFT devices (Figure 7f). (8), (39) Additionally, the appropriate quantity of hydrogen may effectively passivate the interfacial states and improve the performance of TFT devices. Finally, electrical conduction in oxide semiconductors (ZnO) is dominated by electron-trapping sites (Figure 8a). Electron transport may be used to establish trapping sites based on the multiple-trapping-and-releasing paradigm. Before engaging in conduction transport, the majority of electrons occupy the confined state (Figure 8b), and only a tiny fraction of electrons may travel into the transport bands. The increased capacitance of the SbOx dielectric results in a larger electric field, which delivers more energy to electrons. As a result, a high number of electrons occupy the lower-lying localised state readily and are promptly entrapped in the upper-lying localised state, significantly increasing the TFT mobility. [40, 20, 20]

Details are in the caption following the image

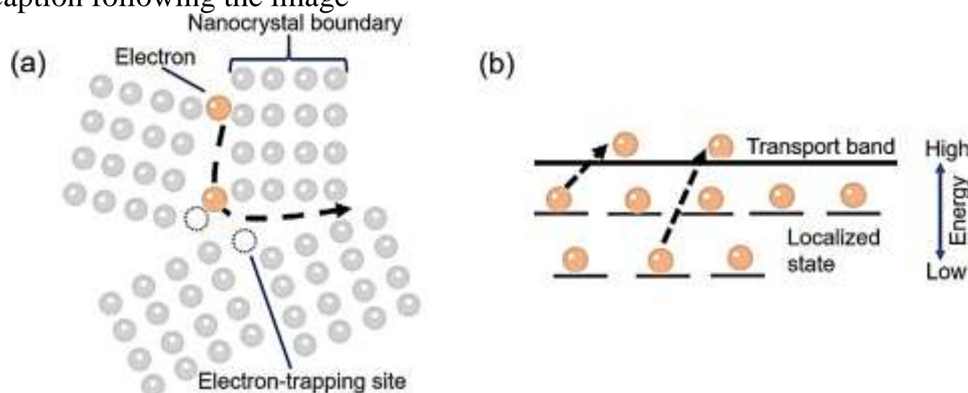

Figure 8: a) Schematic representation of the electron transport mechanism; b) Energy band diagram of oxide semiconductor thin films. SbOx induces a very strong electric field, which makes it simpler to rapidly trap electrons in the upper-lying localised states.

3. CONCLUSION

In summary, SbOx thin films were effectively produced in the temperature range of 80–200 °C utilising a novel mixture of antimony reactants and oxidizers, namely SbCl5, Sb(NMe2)3, H2O, and H2O2. Additionally, the dielectric characteristics of SbOx thin films generated by ALD were thoroughly investigated. The structural and compositional characterisation of thin films using XRD, TEM, AFM, and XRR validates the films' homogeneity, high density, and amorphous nature. Additionally, as shown by ToF-ERDA and XPS, raising the deposition temperature resulted in the deposition of denser and purer SbOx phases. The UPS spectra demonstrate that when the deposition temperature increases, the work function lowers and the Fermi level moves toward the conduction band edge. The kind of precursor and deposition temperature have an effect on the TFT performance of devices. Due of the high bonding energy of MCl, it is easier to create SbO bonds throughout the ALD process at high deposition temperature for SbCl5-based SbOx. Cl may damage the dielectric properties of SbOx thin films, resulting in a large leaking current and a low breakdown electric field. By contrast, the SbOx films based on Sb(NMe2)3 exhibit excellent dielectric characteristics, with a breakdown field of 4 MV cm1 and a high areal capacitance of 200 nF cm2 at 200 °C. ZnO/SbOx thin film transistors were developed to test the efficiency of deposited films in TFT devices. A TFT with a SbOx dielectric layer produced at 200 °C using Sb(NMe2)3 and H2O2 demonstrated the highest performance, including a high of 12.4 cm2 V1 s1, a high Ion/Ioff ratio of 4 108, a sharp SS of 0.22 V dec1, and a low Ntrap of 1.1 1012 eV1 cm2. After applying a 10 V voltage stress for 3600 s, the SbOx–ZnO TFT's Vth is just 1.2 V. The results of this study will aid in the creation of novel microelectronics and applications.

4. EXPERIMENTAL SECTION

Deposition of SbOx Thin Film

On Si and quartz glass substrates, SbOx thin films were formed using a thermal ALD reactor (Veeco Savannah S200) at deposition temperatures of 80, 100, 150, and 200 °C. Antimony reactants SbCl5 and Sb(NMe2)3 were utilised, whereas oxidizers H2O and H2O2 were used. SbCl5 and Sb(NMe2)3 were kept at 40 °C and ambient temperature, respectively, and were pulsed into the reaction chamber by a constant N2 flow. For one ALD deposition cycle (Sb precursor/N2/H2O or H2O2/N2), the optimal pulse and purge periods were 0.15/10/0.5/10 s. There was no interaction between Sb(NMe2)3 and H2O, however both water and H2O2 were capable of oxidising SbCl5 throughout the ALD process.

Device Fabrication

ZnO with a diameter of 16 nm was formed onto 60 nm thick SbOx thin films. Magnetron sputtering was used to deposit Cr/Au electrodes as the source/drain of TFT devices with a channel width (W) of 1000 m and a channel length (L) of 80 m. A metal–insulator–metal (MIM) device was built to study the dielectric characteristics of SbOx. On a heavily doped Si substrate (0.001 cm), a thin coating of SbOx was deposited. Then, using a shadow mask with a diameter of 1 mm, the Cr/Au was deposited as an upper electrode through sputtering. Figure S10 illustrates the MIM schematic (Supporting Information).

Thin Film and Device Characterization

XRR (Philips X'Pert Pro MRD) was used to determine the depth of the thin films. AFM (Bruker Dimension Icon) and field-emission scanning electron microscopy were used to investigate the surface morphology (Sigma 300-ZEISS FESEM). The XPS analysis was performed on a Thermo Scientific K-Alpha+. UPS was done using a Thermo ESCALAB 250Xi system. The resonant line He-I (hv = 21.2 eV) was used to ignite the samples. Each measurement was conducted with the identical bias voltage of 10 V. ToF-ERDA was used to determine the elemental makeup and depth profiles of thin films using a 6.8 MeV 35Cl3+ laser. Using a mirror measurement geometry, the scattering angle was 15° or 20°. Potku software was used to examine the ToF-ERD data. [41] A double-beam spectrophotometer was used to determine the optical transmission (U-3900). The following equations were used to compute the field-effect mobility () and SS:

$ID = (W2LCi\mu)(VGS - Vth)2$ (2)

$SS = dVGSd(\log ID)$ (3)

W and L denote the channel diameter and depth, respectively, Ci denotes the dielectric's area capacitance, Vth denotes the threshold voltage, and VGS denotes the gate voltage. The Tauc model was used to determine the bandgap of the thin films:

$(\alpha \cdot h\nu)2 = A(h\nu - Eg)$ (4)

Here α is the absorption coefficient and A and hν are a constant and the photon energy, respectively.

REFERENCE:

1B. Wang, W. Huang, L. Chi, M. Al-Hashimi, T. J. Marks, A. Facchetti, Chem. Rev. 2018, 118, 5690. CrossrefCASPubMedWeb of Science®Google Scholar
2a) K. Lu, J. Zhang, D. Guo, J. Xiang, Z. Lin, X. Zhang, T. Wang, H. Ning, R. Yao, J. Peng, IEEE Electron Device Lett. 2020, 41, 417;CrossrefCASWeb of Science®Google Scholar
b) J. W. Park, B. H. Kang, H. J. Kim, Adv. Funct. Mater. 2020, 30, 1904632; Wiley Online LibraryCASWeb of Science®Google Scholar
c) A. Liu, H. Zhu, H. Sun, Y. Xu, Y.-Y. Noh, Adv. Mater. 2018, 30, 1706364.
Wiley Online LibraryWeb of Science®Google Scholar
3E. Yarali, C. Koutsiaki, H. Faber, K. Tetzner, E. Yengel, P. Patsalas, N. Kalfagiannis, D. C. Koutsogeorgis, T. D. Anthopoulos, Adv. Funct. Mater. 2019, 30, 1906022.Wiley Online LibraryWeb of Science®Google Scholar
4K. Nomura, H. Ohta, A. Takagi, T. Kamiya, M. Hirano, H. Hosono, Nature 2004, 432, 488.
CrossrefCASPubMedWeb of Science®Google Scholar
5A. T. Oluwabi, A. Katerski, E. Carlos, R. Branquinho, A. Mere, M. Krunks, E. Fortunato, L. Pereira, I. O. Acik, J. Mater. Chem. C 2020, 8, 3730.CrossrefCASWeb of Science®Google Scholar
6N. P. Maity, R. Maity, S. Baishya, High-k Gate Dielectric Materials: Applications with Advanced Metal Oxide Semiconductor Field Effect Transistors (MOSFETs), CRC Press, Boca Raton, FL 2020.Crossref Google Scholar
7M. T. Bohr, R. S. Chau, T. Ghani, K. Mistry, IEEE Spectrum 2007, 44, 29.
CrossrefWeb of Science®Google Scholar
8A. Zeumault, V. Subramanian, Adv. Funct. Mater. 2016, 26, 955.Wiley Online LibraryCASWeb of Science®Google Scholar
9W. Han, P. Huang, L. Li, F. Wang, P. Luo, K. Liu, X. Zhou, H. Li, X. Zhang, Y. Cui, T. Zhai, Nat. Commun. 2019, 10, 4728.
CrossrefPubMedWeb of Science®Google Scholar
10J. Peng, W. Pu, S. Lu, X. Yang, C. Wu, N. Wu, Z. Sun, H. T. Wang, Nano Lett. 2021, 21, 203.CrossrefCASPubMedWeb of Science®Google Scholar
11K. Liu, B. Jin, W. Han, X. Chen, P. Gong, L. Huang, Y. Zhao, L. Li, S. Yang, X. Hu, J. Duan, L. Liu, F. Wang, F. Zhuge, T. Zhai, Nat. Electron. 2021, 4, 906.CrossrefCASWeb of Science®Google Scholar
12X. Ding, J. Yang, C. Qin, X. Yang, T. Ding, J. Zhang, IEEE Trans. Electron Devices 2018, 65, 3283.CrossrefCASWeb of Science®Google Scholar
13A. Liu, H. Zhu, Y.-Y. Noh, Mater. Sci. Eng., R 2019, 135, 85.CrossrefWeb of Science®Google Scholar
14L. Qiang, X. Liang, Y. Pei, R. Yao, G. Wang, Thin Solid Films 2018, 649, 51.CrossrefCASWeb of Science®Google Scholar
15a) J. Yang, X. Yang, Y. Zhang, B. Che, X. Ding, J. Zhang, Mol. Cryst. Liq. Cryst. 2019, 676, 65;CrossrefWeb of Science®Google Scholar
b) J. Zhang, X. Ding, J. Li, H. Zhang, X. Jiang, Z. Zhang, Ceram. Int. 2016, 42, 8115;
CrossrefCASWeb of Science®Google Scholar
c) D. M. Hausmann, R. G. Gordon, J. Cryst. Growth 2003, 249, 251.CrossrefCASWeb of Science®Google Scholar
16S. Kinnunen, K. Arstila, T. Sajavaara, Appl. Surf. Sci. 2021, 546, 148909.CrossrefCASWeb of Science®Google Scholar
17a) J. Sheng, J.-H. Lee, W.-H. Choi, T. Hong, M. Kim, J.-S. Park, J. Vac. Sci. Technol., A 2018, 36, 060801;CrossrefWeb of Science®Google Scholar
b) R. B. Yang, J. Bachmann, M. Reiche, J. W. Gerlach, U. Gösele, K. Nielsch, Chem. Mater. 2009, 21, 2586;CrossrefCASWeb of Science®Google Scholar
c) S. He, A. Bahrami, X. Zhang, I. G. Martínez, S. Lehmann, K. Nielsch, Adv. Mater. Technol. 2021, 2100953;Wiley Online LibraryWeb of Science®Google Scholar
d) J. Yang, Y. Zhang, C. Qin, X. Ding, J. Zhang, IEEE Trans. Electron Devices 2019, 66, 1760.
CrossrefCASWeb of Science®Google Scholar
18M. Laitinen, M. Rossi, J. Julin, T. Sajavaara, Nucl. Instrum. Methods Phys. Res., Sect. B 2014, 337, 55.CrossrefCASWeb of Science®Google Scholar
19a) L. Y. Liang, H. T. Cao, Q. Liu, K. M. Jiang, Z. M. Liu, F. Zhuge, F. L. Deng, ACS Appl. Mater. Interfaces 2014, 6, 2255;CrossrefCASPubMedWeb of Science®Google Scholar
b) F. M. Li, B. C. Bayer, S. Hofmann, J. D. Dutson, S. J. Wakeham, M. J. Thwaites, W. I. Milne, A. J. Flewitt, Appl. Phys. Lett. 2011, 98, 252903;CrossrefCASWeb of Science®Google Scholar
c) X.-H. Zhang, S. P. Tiwari, S.-J. Kim, B. Kippelen, Appl. Phys. Lett. 2009, 95, 312;
Google Scholar

d) R. Sarma, D. Saikia, P. Saikia, P. Saikia, B. Baishya, Braz. J. Phys. 2010, 40, 357;
CrossrefCASWeb of Science®Google Scholar
e) G. Geng, G. Liu, F. Shan, A. Liu, Q. Zhang, W. Lee, B. Shin, H. Wu, Curr. Appl. Phys. 2014, 14, S2;CrossrefWeb of Science®Google Scholar
f) Y. Zhou, N. Kojima, K. Sasaki, J. Phys. D: Appl. Phys. 2008, 41, 175414;
CrossrefWeb of Science®Google Scholar
g) K. Kukli, K. Forsgren, M. Ritala, M. Leskelä, J. Aarik, A. Haårsta, J. Electrochem. Soc. 2001, 148, F227;CrossrefCASWeb of Science®Google Scholar
h) J. Zhang, S. Liu, L. Kong, J. P. Nshimiyimana, X. Hu, X. Chi, P. Wu, J. Liu, W. Chu, L. Sun, Adv. Electron. Mater. 2018, 4, 1700628;Wiley Online LibraryWeb of Science®Google Scholar
i) L. Nyns, J. G. Lisoni, G. Van den Bosch, S. Van Elshocht, J. Van Houdt, Phys. Status Solidi A 2014, 211, 409;Wiley Online LibraryCASWeb of Science®Google Scholar
j) A. Kosola, J. Päiväsaari, M. Putkonen, L. Niinistö, Thin Solid Films 2005, 479, 152.
CrossrefCASWeb of Science®Google Scholar
20J. Yang, Y. Zhang, Q. Wu, C. Dussarrat, J. Qi, W. Zhu, X. Ding, J. Zhang, IEEE Trans. Electron Devices 2019, 66, 3382.CrossrefCASWeb of Science®Google Scholar
21W. J. Lee, S. Bera, Z. Wan, W. Dai, J. S. Bae, T. E. Hong, K. H. Kim, J. H. Ahn, S. H. Kwon, J. Am. Ceram. Soc. 2019, 102, 5881.Wiley Online LibraryCASWeb of Science®Google Scholar
22A. Sharma, V. Longo, M. A. Verheijen, A. A. Bol, W. M. M. Kessels, J. Vac. Sci. Technol., A 2017, 35, 01B130.CrossrefWeb of Science®Google Scholar
23L. P. Bakos, J. Mensah, K. László, B. Parditka, Z. Erdélyi, E. Székely, I. Lukács, Z. Kónya, C. Cserháti, C. Zhou, J. Mater. Chem. C 2020, 8, 6891.CrossrefCASWeb of Science®Google Scholar
24a) J. F. Conley, Y. Ono, D. J. Tweet, W. Zhuang, R. Solanki, J. Appl. Phys. 2003, 93, 712;
CrossrefCASWeb of Science®Google Scholar
b) H. J. Lee, J. H. Hwang, J.-Y. Park, S. W. Lee, ACS Appl. Electron. Mater. 2021, 3, 999.
CrossrefCASGoogle Scholar
25C. B. Musgrave, R. G. Gordon, Future Fab Int. 2005, 18, 126.Google Scholar
26J. H. Park, Y. B. Yoo, K. H. Lee, W. S. Jang, J. Y. Oh, S. S. Chae, H. K. Baik, ACS Appl. Mater. Interfaces 2013, 5, 410.CrossrefCASPubMedWeb of Science®Google Scholar
27Z. Guo, A. Liu, Y. Meng, C. Fan, B. Shin, G. Liu, F. Shan, Ceram. Int. 2017, 43, 15194.
CrossrefCASWeb of Science®Google Scholar
28a) Y. Wang, L. Jiang, Y. Liu, D. Tang, F. Liu, Y. Lai, J. Alloys Compd. 2017, 727, 469;
CrossrefCASWeb of Science®Google Scholar
b) Y. Huang, P. Ruiz, J. Phys. Chem. B 2005, 109, 22420.CrossrefCASPubMedWeb of Science®Google Scholar
29Y. Widjaja, C. B. Musgrave, J. Chem. Phys. 2002, 117, 1931.CrossrefCASWeb of Science®Google Scholar
30a) Y. Shao, X. Wu, M. N. Zhang, W. J. Liu, S. J. Ding, Nanoscale Res. Lett. 2019, 14, 122;
CrossrefPubMedWeb of Science®Google Scholar
b) Y. Wu, L. Lan, P. He, Y. Lin, C. Deng, S. Chen, J. Peng, Appl. Sci. 2021, 11, 4393.
CrossrefCASWeb of Science®Google Scholar
31C.-E. Kim, J. M. Skelton, A. Walsh, A. Soon, J. Mater. Chem. C 2015, 3, 11349.
CrossrefCASWeb of Science®Google Scholar
32S. S. Barala, V. S. Bhati, M. Kumar, Thin Solid Films 2017, 639, 107.CrossrefCASWeb of Science®Google Scholar
33L. Zuo, X. Jiang, L. Yang, M. Xu, Y. Nan, Q. Yan, H. Chen, Appl. Phys. Lett. 2011, 99, 183306.CrossrefCASWeb of Science®Google Scholar
34a) P. M. Jordan, D. K. Simon, F. P. G. Fengler, T. Mikolajick, I. Dirnstorfer, Energy Procedia 2015, 77, 91;CrossrefCASGoogle Scholar
b) Y. J. Kim, D. Lim, H. H. Han, A. S. Sergeevich, Y.-R. Jeon, J. H. Lee, S. K. Son, C. Choi, Microelectron. Eng. 2017, 178, 284.CrossrefCASWeb of Science®Google Scholar
35K. Kukli, M. Ritala, T. Sajavaara, J. Keinonen, M. Leskelä, Thin Solid Films 2002, 416, 72.
CrossrefCASWeb of Science®Google Scholar
36a) J. Robertson, B. Falabretti, Mater. Sci. Eng., B 2006, 135, 267;CrossrefCASWeb of Science®Google Scholar
b) M. Liu, Q. Fang, G. He, L. Li, L. Q. Zhu, G. H. Li, L. D. Zhang, Appl. Phys. Lett. 2006, 88, 192904.CrossrefCASWeb of Science®Google Scholar
37C. R. Kagan, A. Paul, Thin-Film Transistors, CRC Press, New York, NY 2003.Google Scholar
38M. Napari, T. N. Huq, D. J. Meeth, M. J. Heikkila, K. M. Niang, H. Wang, T. Iivonen, H. Wang, M. Leskela, M. Ritala, A. J. Flewitt, R. L. Z. Hoye, J. L. MacManus-Driscoll, ACS Appl. Mater. Interfaces 2021, 13, 4156.CrossrefCASPubMedWeb of Science®Google Scholar

39A. Liu, H. Zhu, Y.-Y. Noh, Adv. Funct. Mater. 2020, 30, 2002625.Wiley Online LibraryCASWeb of Science®Google Scholar
40E. Lee, J. Ko, K.-H. Lim, K. Kim, S. Y. Park, J. M. Myoung, Y. S. Kim, Adv. Funct. Mater. 2014, 24, 4689.Wiley Online LibraryCASWeb of Science®Google Scholar
41K. Arstila, J. Julin, M. I. Laitinen, J. Aalto, T. Konu, S. Kärkkäinen, S. Rahkonen, M. Raunio, J. Itkonen, J. P. Santanen, Nucl. Instrum. Methods Phys. Res., Sect. B 2014, 331, 34.
CrossrefCASWeb of Science®Google Scholar